Drops on the Underside of a Slightly Inclined Wet Substrate Move Too Fast to Grow

Etienne Jambon-Puillet,[1] Pier Giuseppe Ledda,[2] François Gallaire,[2] and P.-T. Brun[1]

[1]*Department of Chemical and Biological Engineering,
Princeton University,Princeton, New-Jersey 08540, USA*
[2]*Laboratory of Fluid Mechanics and Instabilities, École Polytechnique Fédérale de Lausanne, Lausanne, CH-1015, Switzerland*
(Dated: August 2, 2021)

Pendant drops suspended on the underside of a wet substrate are known to accumulate fluid from the surrounding thin liquid film, a process that often results in dripping. The growth of such drops is hastened by their ability to translate over an otherwise uniform horizontal film. Here we show that this scenario is surprisingly reversed when the substrate is slightly tilted (≈ 2 deg) ; drops become too fast to grow and shrink over the course of their motion. Combining experiments and numerical simulations, we rationalize the transition between the conventional growth regime and the previously unknown decay regime we report. Using an analytical treatment of the Landau-Levich meniscus that connects the drop to the film, we quantitatively predict the drop dynamics in the two flow regimes and the value of the critical inclination angle where the transition between them occurs.

Anyone who has applied paint to a ceiling knows that thin liquid coatings can spontaneously destabilize and accumulate into an array of pendant drops [1, 2]. While interfacial instabilities can be harnessed to build structures akin to geomorphic patterns [3–8], the Rayleigh-Taylor instability in films is more commonly seen as undesirable, e.g. jeopardizing the uniformity of coatings [9]. Worse, as they grow, instability-mediated drops can drip and pollute the space underneath, with potentially severe consequences for engineering constructs [10, 11]. As such, the Rayleigh-Taylor instability in thin viscous films has been extensively studied [1, 2, 12–14] and diverse strategies have been proposed to prevent the formation of drops [15–21]. Linear stability analysis for this class of problems is therefore well established, while insights in the drop patterns formed by the instability have been provided using weakly nonlinear developments [2]. Yet, our understanding of fully formed pendant drops and their transition to dripping remains sparse [22] owing to the difficulties of modeling the fully non-linear long-term dynamics. In this Letter, we focus on a single pendant drop (see Fig. 1), a problem that remains analytically tractable while retaining a rich physics.

Pendant drops under uniformly coated films are capable of steady translation, even in the theoretical limit of a perfectly horizontal substrate [22]. Over the course of their trajectory, these drops accumulate more fluid from the surrounding thin film than if they were stationary [22], thereby reaching the critical size leading to dripping [4] faster than immobile drops. Here, using experiments, numerical simulations and theory, we show that increasing the drop velocity by slightly tilting the substrate surprisingly prevents dripping. Past a critical inclination, the film left by the drop in its wake is thicker than the one absorbed by the drop in its front. This negative balance depletes the volume of fluid in the drop, which shrinks, thereby avoiding dripping. Through an analysis of the Landau-Levich meniscus at the edge of the drop, we unveil the physics at play in these drops that are too fast to grow and predict analytically their dynamics and the transition between the two aforementioned flow regimes.

Our experiment is schematized in Fig. 1. Silicone oil (density $\rho = 971$ kg/m^3, surface tension $\gamma = 20.3$ mN/m, viscosity $\eta = 1.13$ Pa.s) is spin-coated on a flat glass substrate to produce a film of uniform thickness h_0 (measured by weighting the sample). The substrate is then flipped and mounted onto a rotating arm while a droplet is applied on the film with a micropipette. The resulting pendant drop has an initial amplitude $A_0 \sim \ell_c$ where $\ell_c = \sqrt{\gamma/(\rho g)}$ denotes the capillary length and g denotes the acceleration of gravity. The substrate is then tilted by an angle α and the dynamics is recorded (see SM section I for details [23]). Note that the initial coating is sufficiently thin not to destabilize via the Rayleigh-Taylor instability over the course of our experiment [2]. The film thickness is therefore assumed to be uniform and constant far from the drop.

Fig. 2(a) shows a chronophotography of an experiment performed with a nearly horizontal substrate ($\alpha = 0.9°$). As evident from the figure, the drop translates by several times its diameter over the course of the experiment while both the drop speed U and amplitude A increase. In Fig. 2(b), we show an experiment nearly identical to (a), except for that the inclination angle is slightly higher ($\alpha = 3.4°$). As expected, the drop initially moves faster. However, unlike the lower inclination case, it progressively shrinks and decelerates. In Fig. 3 we plot the amplitude $A(t)$ and position $x(t)$ of drops sliding over films of similar thickness ($h_0 \approx 89\ \mu$m) but with different inclination angles α. While the drop accelerates and grows for the three smallest angles, the situation is reversed for the two largest angles. The inclination $\alpha_c \approx 2°$ appears to be the critical angle, α_c, where the drop amplitude and speed are constant
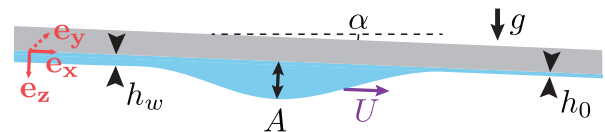

FIG. 1. Schematic of a pendant drop of amplitude A sliding with velocity U under a substrate pre-wetted with a film of thickness h_0 and inclined by an angle α.
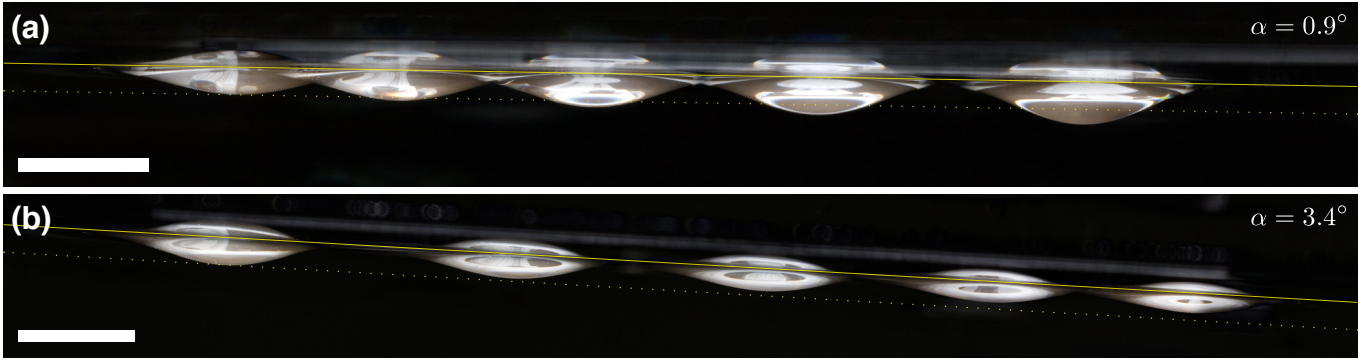
FIG. 2. Chronophotographies of two experiments at low **(a)** and high **(b)** inclination angles with $h_0 \approx 89$ μm (scale bars are 5 mm). The interval between pictures is 9 and 3.75 min, respectively. The pictures include the reflexion of the drop on the substrate. The solid lines indicate the position of the substrate. The dotted lines mark the initial amplitudes of the drops $A_0 = \{1.03, 1.16\}$ mm.
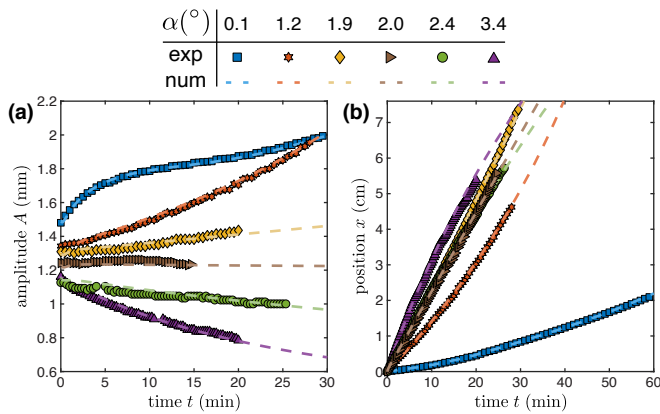

FIG. 3. Shown is the amplitude $A(t)$ **(a)** and position $x(t)$ **(b)** of drops sliding under a film of thickness $h_0 \approx 89$ μm at different inclination angles α (see legend). Markers indicate experiments and dashed lines indicate numerical simulations.

($U \approx 2.3$ mm/min). Movie S1 displays similar observations for $h_0 \approx 112$ μm. Modifying the film thickness changes the value of α_c, as well as the timescale of the experiment. Increasing the drop initial amplitude A_0 appears to speed-up the dynamics but does not change its outcome (see SM section II [23]) .

We turn to numerical simulations to rationalize these two flow regimes. Owing to the dimensions of the problem we use the lubrication approximation to describe the evolution of the position of the interface $h(x,y,t)$ [1] but retain the full fledged expression of the curvature κ [14, 24]. In the Cartesian frame aligned with the substrate (see Fig. 1), we obtain the following dimensionless thin-film equation after rescaling x and y using $\ell_c/\sqrt{\cos \alpha}$, h using the coating thickness far from the drop h_0, and t using $\tau = \eta \gamma/ \left(h_0^3 \rho^2 g^2 \cos^2 \alpha \right)$:

$$\partial_{\bar{t}} \bar{h} + \tilde{\alpha} \bar{h}^2 \partial_{\bar{x}} \bar{h} + (1/3) \bar{\nabla} \cdot \left[\bar{h}^3 \left(\bar{\nabla} \bar{h} + \bar{\nabla} \bar{\kappa} \right) \right] = 0,$$

$$\bar{\kappa} = \bar{\nabla} \cdot \left[\bar{\nabla} \bar{h} \Big/ \sqrt{1 + \left(h_0 \sqrt{\cos \alpha}/\ell_c \right)^2 \left(\bar{\nabla} \bar{h} \right)^2} \right], \quad (1)$$

where a bar indicates rescaled variable. Note that the inclination of the substrate is captured by $\tilde{\alpha} = \frac{\ell_c \tan \alpha}{h_0 \sqrt{\cos \alpha}} \approx \frac{\ell_c \alpha}{h_0}$.

We solve eq. (1) with the finite element software COMSOL on a rectangular domain with periodic boundary conditions and the initial condition $\bar{h}(\bar{x}, \bar{y}, 0) = 1 + h_d(\bar{x}, \bar{y})/h_0$. Here, $h_d(\bar{x}, \bar{y})/\ell_c$ is the dimensionless profile of a static pendant drop obtained by integrating the Young-Laplace equation numerically (see SM section I for numerical details [23]). In Movie S2 we report typical numerical results, which appear qualitatively similar to experiments, i.e. predicting growth and ultimately dripping at low inclination angles and the opposite at higher angles. In Fig. 3 we show the evolution of the drop amplitude $A(t)$ and position $x(t)$ obtained numerically with the parameters corresponding to the aforementioned experiments within their uncertainty ($\Delta h_0 = 7$ μm, $\Delta \alpha = 0.15°$). The agreement between experiments and numerics is favorable thereby validating our simulations.

Leveraging our simulations we investigate the physics setting the value of the critical angle α_c. In Fig. 4(a) we plot side-by-side the log of the dimensionless film thickness $h(x,y)/h_0$ for two drops, each of which corresponds to a given flow regime. The two situations only differ in the value of the dimensionless inclination angle $\tilde{\alpha}$. Yet, their respective wakes are qualitatively different. In particular, the wake thickness h_w appears to be mostly greater than h_0 for large inclinations and lower than h_0 for small inclinations. This sizable difference plays a key role in defining the flow regimes. Along its trajectory, a drop indeed absorbs the uniform film laying at its front and releases liquid in its wake. The contribution from the Rayleigh-Taylor instability being negligible (see Fig. S3 in SM [23]), the change in volume of the drop is $\partial_x V \approx \int_{-R}^{R} (h_0 - h_w(y)) \, \mathrm{d}y$ with R the drop radius. The drop shrinks if $\partial_x V < 0$, i.e. if the average thickness left in the wake is less than h_0 as seen for the greater values of the inclination. The structure of the wake is thus key for rationalizing the transition between the two flow regimes. This numerical observation is confirmed in experiments: as evident from Fig. 4(b) the wake is thinner than h_0 for $\alpha < \alpha_c$ and thicker for $\alpha > \alpha_c$ (see
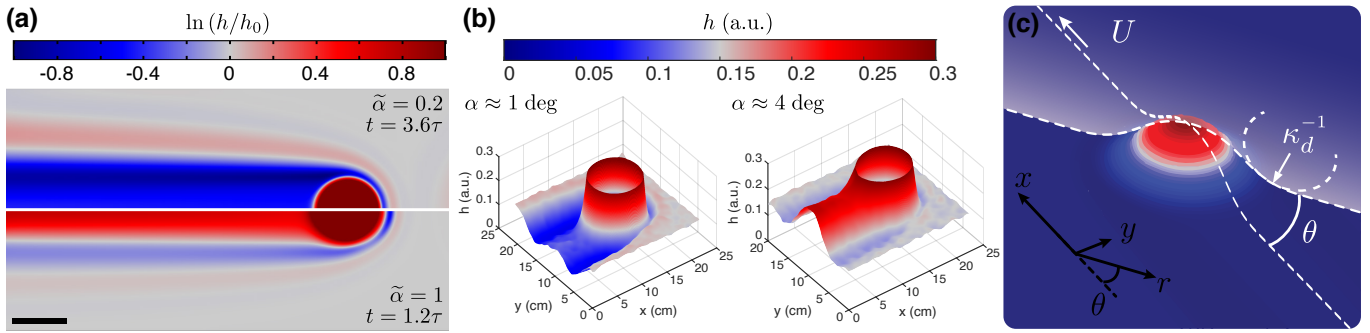
FIG. 4. **(a)** Thickness map for two simulations with identical initial drops ($A_0/\ell_c = 1.05$, $h_0/\ell_c = 0.04$) but different inclination angles $\widetilde{\alpha}$ (position $x = 37.4\ell_c$). Scale bar $5\ell_c$. **(b)** Thickness profiles inferred from experiments conducted with dyed oil at low and high inclination angles ($A_0/\ell_c \approx 0.8$, $h_0 \approx 85~\mu$m). **(c)** Three dimensional schematics of the drop introducing the polar coordinates $\{r, \theta\}$, and curvature κ_d.

details in SM section I [23]).

We model the variation in thickness across the wake using an approach analogous to that used in Landau-Levich and Bretherton problems. We treat our problem in the polar coordinate system centered on the drop apex [see Fig. 4(c)]. Focusing on the matching region between the drop and the film, we expect the radial curvature to vary rapidly and dominate the pressure gradient [22]. Consequently, we neglect the advection and gravity terms in the meniscus such that eq. (1) reduces to a radial Landau-Levich equation (see SM section III [23]). Therefore, we treat the wake as a collection of two-dimensional radial Landau-Levich films, where the projected speed $U\cos(\theta)$ is the effective deposition speed. In this framework, we obtain [25]

$$h_w(\theta) \approx 1.34\kappa_d^{-1}\cos(\theta)^{2/3}\mathrm{Ca}^{2/3}. \tag{2}$$

Here κ_d is the curvature at the edge of the drop, which is assumed to remain close to that of a static pendant drop $\kappa_d \approx 0.28A/\ell_c^2$ (see SM section III [23]), and $\mathrm{Ca} = \eta U/\gamma$ is the capillary number of the problem. Note that the drop speed $U(t)$ and amplitude $A(t)$ are a priori unknown and depend on the drop initial profile, the film thickness and the inclination of the substrate. Varying the dimensionless parameters of the problem (A_0/ℓ_c, h_0/ℓ_c and $\widetilde{\alpha}$) we generate a large data set of simulations to assess the validity of our model.

In Fig. 5(a) we plot the wake profile in the transverse direction $h_w(y)$ for a given drop and film at different inclinations angles [the wake is quasi-invariant in the x direction, see Fig. 4(a)]. We first focus on the angular dependence by rescaling the data by $h_w(y = 0)$. As shown in Fig. 5(b), the profiles collapse in the central region of the wake defined as $-R < y < R$ with R the drop radius. The resulting master curve matches our theoretical prediction $h_w(\theta)/h_w(0) = \cos(\theta)^{2/3}$ with no fitting parameter [see eq. (2)]. We then compare our prediction for $h_w(0)$ to data from all our simulations in Fig. 5(c). Note that each simulation provides multiple data points as A and U are both function of time and thus vary over the course of a simulation. The resulting collapse and overall favorable agreement with eq. (2) confirms the validity of
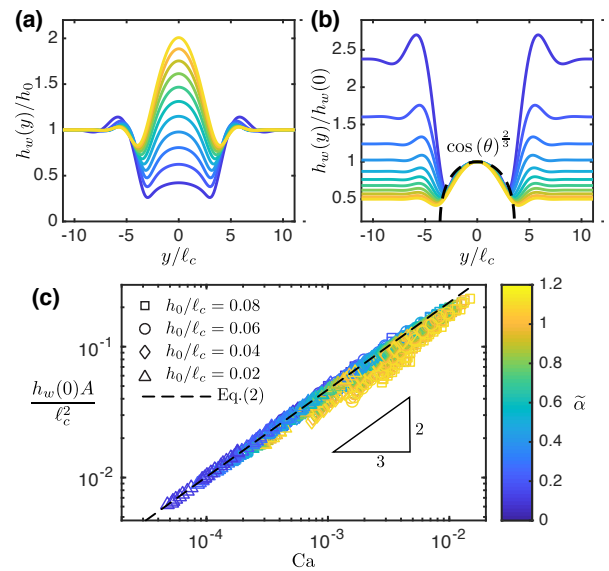

FIG. 5. **(a)** Wake profile $h_w(y)/h_0$ taken $\approx 6\ell_c$ behind a drop [23] for different inclination angles $\widetilde{\alpha}$ [color coded see **(c)**], $A_0/\ell_c = 1.4$ and $h_0/\ell_c = 0.04$. **(b)** Same data rescaled by the central thickness $h_w(0)$. The black dashed line derives from eq. (2): $h_w(y)/h(0) = \cos(\theta)^{2/3} = \cos(\arcsin(y/R))^{2/3}$. **(c)** Dimensionless thickness in the center of the wake $h_w(0)A/\ell_c^2$ as a function of the capillary number Ca for our 176 simulations. The color codes $\widetilde{\alpha}$, the symbols code h_0/ℓ_c and the black dashed line corresponds to eq. (2): $y = 1.34/0.28x^{2/3}$.

our approach. Note that the agreement becomes less favorable when $\widetilde{\alpha}$ and h_0/ℓ_c increase, a result consistent with the approximations made in our model (negligible advection in the meniscus and static pendant drop shape, see SM section III [23]).

Using eq. (2), we evaluate the amount of liquid deposited in the wake $\int_{-R}^{R} h_w(y)\mathrm{d}y = Rh_w(0)\int_{-\pi/2}^{\pi/2}\cos(\theta)^{5/3}\mathrm{d}\theta$ and obtain the drop growth rate

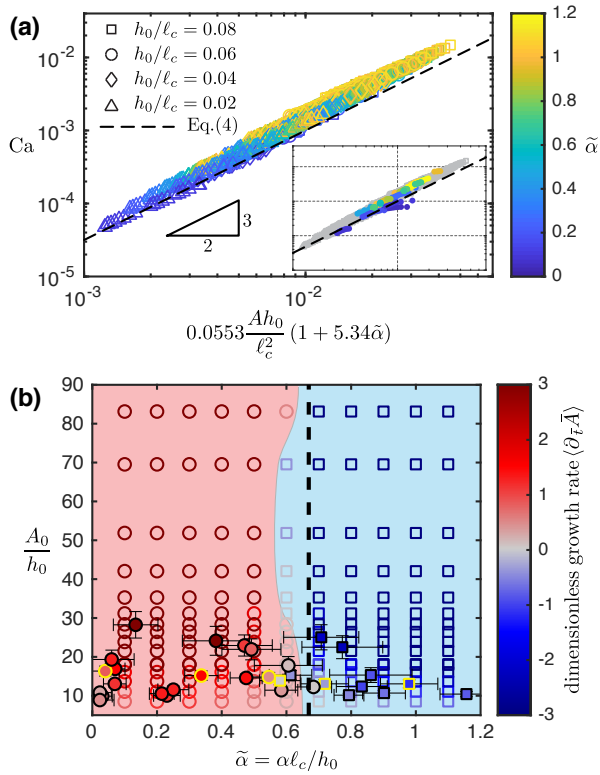$$\partial_x V \approx R\left(2h_0 - 7.91\ell_c^2\mathrm{Ca}^{2/3}/A\right). \tag{3}$$

FIG. 6. **(a)** Drop dimensionless speed Ca compared to our theory [eq. (4)]. Our 176 simulations are shown, the color codes $\widetilde{\alpha}$, the symbols code h_0/ℓ_c and the black dashed line is our prediction $y = x^{3/2}$. Inset: Same plot including experimental data ($0.03 < h_0/\ell_c < 0.1$). The numerics are drawn in light grey for clarity. **(b)** State diagram for the drop growth-decay. Symbols are colored according to the dimensionless growth rate averaged over the experiment/simulation $\langle \partial_{\bar{t}}\bar{A}\rangle$, circles represent growth ($\langle \partial_{\bar{t}}\bar{A}\rangle > 0$) while squares represent decay ($\langle \partial_{\bar{t}}\bar{A}\rangle < 0$). Experimental results are shown as filled symbols while numerical results are open symbols. The experiments of Fig. 3 are circled in yellow. The background color is a guide to the eye and the dashed black line is our theory $\widetilde{\alpha}_c \approx 0.67$.

Next, we derive an expression for Ca in order to close the problem.

To obtain the drop speed, we perform a force balance on the drop [26]. The force driving the motion of the drop derives from the change in gravitational energy $E_p = \rho g V z_c$, with z_c the altitude of the drop center of mass. Defining $F_g = -\partial_x E_p$ we find $F_g \approx \rho g V \alpha + 2\rho g z_c R h_0 - 7.91\gamma R z_c \mathrm{Ca}^{2/3}/A$. While the first term in the expression of F_g is conventional, the other two terms originate from the change of volume of the drop $\partial_x V$ in eq. (3). The motion of the drop is resisted by viscous stresses in the film. The flow being significant only around the drop and the meniscus being the thinnest part of that region, we anticipate the meniscus to be the main source of dissipation. The corresponding viscous force per unit length is $f_v(\theta) = 4.94\gamma(\mathrm{Ca}\cos\theta)^{2/3}$ [25]. Integrating along the drop contour, the total friction force is $\mathbf{F_v} = \int_{-\pi/2}^{\pi/2} f_v(\theta)\left(\cos\theta\,\mathbf{e_x} + \sin\theta\,\mathbf{e_y}\right) R\,d\theta \approx 8.31\gamma R \mathrm{Ca}^{2/3}\mathbf{e_x}$.

Assuming that the drop shape remains close to that of a static pendant drop we have $z_c \approx 0.29A$, $R \approx 3.58\ell_c$ and $V \approx 0.89AR^2$ (see SM section III [23] for the derivation of all the prefactors). Balancing F_g and $F_v = \mathbf{F_v}.\mathbf{e_x}$, we obtain:

$$\mathrm{Ca}^{2/3} = 0.0553\frac{Ah_0}{\ell_c^2}\left(1 + 5.34\widetilde{\alpha}\right). \tag{4}$$

In Fig. 6(a) we compare the drop speed obtained in simulations with eq. (4) and find favorable agreement without any fitting parameter. Likewise, we show in Inset of Fig. 6(a) that eq. (4) also captures our experiments. Note that, the agreement becomes less favorable when $\widetilde{\alpha}$ and h_0/ℓ_c increase, as expected from the deterioration of our model's assumptions (static pendant drop shape and negligible advection in the meniscus, see SM section III [23]).

We now leverage our results and combine eq. (3) and eq. (4) to derive the drop growth rate $\partial_x V$ and subsequently integrate this expression over time to obtain the drop dimensionless amplitude

$$\frac{\bar{A}(\bar{t})}{\bar{A}_0} = \left(1 - \frac{1}{2}\mathrm{f}(\widetilde{\alpha})\bar{A}_0^{1/2}\bar{t}\right)^{-2} \tag{5}$$

with $\mathrm{f}(\widetilde{\alpha}) = (0.0065 - 0.0097\widetilde{\alpha})(1 + 5.34\widetilde{\alpha})^{3/2}$ (see SM section III [23]). In Fig. S5(a) we show that eq. (5) compares favorably with experiments without fitting parameters. The value of critical inclination is obtained solving for the root of f, yielding $\widetilde{\alpha}_c \approx 0.67$. In Fig. 6(b) we show the combined experimental and numerical state diagram for the drop dynamics, where the two flow regimes are apparent. As predicted by our model, the transition occurs at a roughly constant critical angle $\widetilde{\alpha}_c \approx 0.6$ in good agreement with our estimate.

In summary, using experiments and numerical simulations, we have revealed a transition from growth to decay for pendant drops sliding under slightly inclined pre-wet substrates. This transition, which occurs at a surprisingly low angle, is governed by the amount of fluid left in the wake of the drop. As the inclination angle increases, the drop becomes too fast to grow and its volume is slowly depleted. We have rationalized this complex non-linear problem with an analytically tractable Landau-Levich model that accurately predicts the drop dynamics in the two regimes, in spite of the approximations introduced in its derivation. Note that on longer time scales the Rayleigh-Taylor instability will eventually influence the dynamics of drops that do not drip. Although this situation is beyond the scope of the present study, preliminary results indicate that the wake forms lenses that are later absorbed by the drop (see SM section II [23] and Movie. S3). Yet, no dripping is observed which suggest that the critical angle we have introduced remains accurate. As such, our results could find application in dripping prevention for drops directly deposited on substrates, e.g. in coating and printing technologies [27]. Additionally, our results could be extended to control and transport pendant drops via carefully crafted substrate topography. Finally, our analysis could be

generalized to model the dynamics of sliding liquid plugs in pre-wetted channels [28] and sliding liquid bridges between pre-wetted substrates [29, 30].

---

[1] S. G. Yiantsios and B. G. Higgins, Rayleigh–taylor instability in thin viscous films, Physics of Fluids A: Fluid Dynamics **1**, 1484 (1989).

[2] M. Fermigier, L. Limat, J. E. Wesfreid, P. Boudinet, and C. Quilliet, Two-dimensional patterns in rayleigh-taylor instability of a thin layer, Journal of Fluid Mechanics **236**, 349–383 (1992).

[3] R. T. Weitz, L. Harnau, S. Rauschenbach, M. Burghard, and K. Kern, Polymer nanofibers via nozzle-free centrifugal spinning, Nano Letters **8**, 1187 (2008).

[4] J. Marthelot, E. F. Strong, P. M. Reis, and P.-T. Brun, Designing soft materials with interfacial instabilities in liquid films, Nature Communications **9**, 4477 (2018).

[5] E. Jambon-Puillet, M. Royer Piéchaud, and P.-T. Brun, Elastic amplification of the rayleigh-taylor instability in solidifying melts, Proceedings of the National Academy of Sciences **118** (2021).

[6] N. Ribe, A. Davaille, and U. Christensen, Fluid dynamics of mantle plumes, in Mantle Plumes: A Multidisciplinary Approach, edited by J. R. R. Ritter and U. R. Christensen (Springer Berlin Heidelberg, Berlin, Heidelberg, 2007) pp. 1–48.

[7] C. Camporeale and L. Ridolfi, Hydrodynamic-driven stability analysis of morphological patterns on stalactites and implications for cave paleoflow reconstructions, Phys. Rev. Lett. **108**, 238501 (2012).

[8] U. Dutta, A. Baruah, and N. Mandal, Role of source-layer tilts in the axi-asymmetric growth of diapirs triggered by a Rayleigh–Taylor instability, Geophysical Journal International **206**, 1814 (2016).

[9] S. J. Weinstein and K. J. Ruschak, Coating flows, Annual Review of Fluid Mechanics **36**, 29 (2004).

[10] R. Kaita, L. Berzak, D. Boyle, T. Gray, E. Granstedt, G. Hammett, C. M. Jacobson, A. Jones, T. Kozub, H. Kugel, B. Leblanc, N. Logan, M. Lucia, D. Lundberg, R. Majeski, D. Mansfield, J. Menard, J. Spaleta, T. Strickler, J. Timberlake, J. Yoo, L. Zakharov, R. Maingi, V. Soukhanovskii, K. Tritz, and S. Gershman, Experiments with liquid metal walls: Status of the lithium tokamak experiment, Fusion Engineering and Design **85**, 874 (2010).

[11] G. G. van Eden, V. Kvon, M. C. M. van de Sanden, and T. W. Morgan, Oscillatory vapour shielding of liquid metal walls in nuclear fusion devices, Nature Communications **8**, 192 (2017).

[12] L. Limat, P. Jenffer, B. Dagens, E. Touron, M. Fermigier, and J. Wesfreid, Gravitational instabilities of thin liquid layers: dynamics of pattern selection, Physica D: Nonlinear Phenomena **61**, 166 (1992).

[13] H. N. Yoshikawa, C. Mathis, S. Satoh, and Y. Tasaka, Inwardly rotating spirals in a nonoscillatory medium, Phys. Rev. Lett. **122**, 014502 (2019).

[14] G. Lerisson, P. G. Ledda, G. Balestra, and F. Gallaire, Instability of a thin viscous film flowing under an inclined substrate: steady patterns, Journal of Fluid Mechanics **898**, A6 (2020).

[15] J. M. Burgess, A. Juel, W. D. McCormick, J. B. Swift, and H. L. Swinney, Suppression of dripping from a ceiling, Phys. Rev. Lett. **86**, 1203 (2001).

[16] V. Lapuerta, F. J. Mancebo, and J. M. Vega, Control of rayleigh-taylor instability by vertical vibration in large aspect ratio containers, Phys. Rev. E **64**, 016318 (2001).

[17] A. Alexeev and A. Oron, Suppression of the rayleigh-taylor instability of thin liquid films by the marangoni effect, Physics of Fluids **19**, 082101 (2007).

[18] R. Cimpeanu, D. T. Papageorgiou, and P. G. Petropoulos, On the control and suppression of the rayleigh-taylor instability using electric fields, Physics of Fluids **26**, 022105 (2014).

[19] P. H. Trinh, H. Kim, N. Hammoud, P. D. Howell, S. J. Chapman, and H. A. Stone, Curvature suppresses the rayleigh-taylor instability, Physics of Fluids **26**, 051704 (2014).

[20] P.-T. Brun, A. Damiano, P. Rieu, G. Balestra, and F. Gallaire, Rayleigh-taylor instability under an inclined plane, Physics of Fluids **27**, 084107 (2015).

[21] G. Balestra, N. Kofman, P.-T. Brun, B. Scheid, and F. Gallaire, Three-dimensional rayleigh–taylor instability under a unidirectional curved substrate, Journal of Fluid Mechanics **837**, 19–47 (2018).

[22] J. R. Lister, J. M. Rallison, and S. J. Rees, The nonlinear dynamics of pendent drops on a thin film coating the underside of a ceiling, Journal of Fluid Mechanics **647**, 239–264 (2010).

[23] See Supplemental Material at http://link.aps.org/supplemental/10.1103/PhysRevLett.127.044503 for experimental and numerical methods, additional experimental and numerical results and more details about the model and its limitations.

[24] S. D. R. Wilson, The drag-out problem in film coating theory, Journal of Engineering Mathematics **16**, 209 (1982).

[25] I. Cantat, Liquid meniscus friction on a wet plate: Bubbles, lamellae, and foams, Physics of Fluids **25**, 031303 (2013).

[26] P. Aussillous and D. Quéré, Bubbles creeping in a viscous liquid along a slightly inclined plane, Europhysics Letters (EPL) **59**, 370 (2002).

[27] S. Kumar, Liquid transfer in printing processes: Liquid bridges with moving contact lines, Annual Review of Fluid Mechanics **47**, 67 (2015).

[28] J. Bico and D. Quéré, Self-propelling slugs, Journal of Fluid Mechanics **467**, 101–127 (2002).

[29] E. Reyssat, Drops and bubbles in wedges, Journal of Fluid Mechanics **748**, 641–662 (2014).

[30] G. M. N. Balestra, Pattern formation in thin liquid films: From coating-flow instabilities to microfluidic droplets, Ph.D. thesis, Lausanne (2018).

Supplemental Material

Etienne Jambon-Puillet,[1] Pier Giuseppe Ledda,[2] François Gallaire,[2] and P.-T. Brun[1]

[1]*Department of Chemical and Biological Engineering,*
Princeton University,Princeton, New-Jersey 08540, USA
[2]*Laboratory of Fluid Mechanics and Instabilities, École Polytechnique Fédérale de Lausanne, Lausanne, CH-1015, Switzerland*
(Dated: July 5, 2021)

In this supplementary document, we provide experimental and numerical methods, additional experimental and numerical results and more details about the model and its limitations.

I. METHODS

Experiments. Silicone oil v1000 (Gelest DMS-T31) dyed in black was used in our experiments. The oil-dye viscosity $\eta = 1.13$ Pa.s was measured in a rheometer (Anton Paar MCR 301) and its surface tension $\gamma = 20.3$ mN/m with the pendant drop method, both at room temperature $T = 21°$C. To prepare the uniform coating h_0, the edges of a rectangular flat, float glass plate (130x90x1.8 mm) were first covered with tape over a width of ≈ 1 cm. Oil was then spin-coated (Laurell WS-650Mz-23NPPB) on the plate and the tape subsequently pealed to remove the edge bead that forms during spin-coating. The plate was then weighted to determine the film thickness $h_0 = m/(\rho S)$ with m the film mass, $\rho = 971$ kg/m^3 the oil density, and S the surface area not covered by the tape (measured with a camera). The experimental uncertainties on the weight measurement translates to a thickness uncertainty $\Delta h_0 \approx \pm 7$ μm. The film thickness was determined for each experiments but most of them were done with similar spin-coating settings leading films thicknesses fluctuating around $h_0 \approx \{55, 89, 110\}$ μm.

The coated plate was then attached upside-down with a magnet to an arm mounted on a rotation stage which has been pre-leveled with a bubble level. Using a micropipette, a drop of oil was injected on the upside down plate. Since a significant portion of the injected oil dripped along the upside down pipette tip, the injected volume was difficult to control precisely (~ 50 μL) leading to drops with various initial amplitudes $0.5 < A_0/\ell_c < 1.46$. The arm was then rotated to the desired angle α. The rotation stage being precise, the uncertainty on the angle α is mostly determined by the leveling step. To gauge it, we recorded the motion of a drop at 'zero' angle for each set of experiments. Although there was a residual tilt in both the x and y direction, we were able to fit the drop dynamics with the numerics only tilted in one direction. The fitted value of $|\alpha_0| = 0.1 - 0.3°$ was then used to correct the zero angle for the following experiments of the set and sets the angle uncertainty $\Delta \alpha \approx \pm 0.15°$.

The drop dynamics was recorded from the side and the bottom with two synchronized cameras. The field of view and resolution were of the order of $\{6.5$ cm, 10 μm/pix$\}$ for the side view and $\{10$ cm, 16 μm/pix$\}$ for the bottom view. The duration of an experiment varying between 20 min and 5h, the time interval between pictures were adjusted accordingly between 15s and 4 min. The drop amplitude was measured from the side view while the drop position was measured

from the bottom view since drops at low angles can move out of plane of the side view. For the experiments shown in Fig. 4b, a much higher concentration of dye was used to visualize the wake. The thickness profiles were then extracted from experimental images using Beer-Lambert's law, i.e. $h(x,y) \sim \ln(I(x,y)/I_0(x,y))$ with I the pixel intensity of the image including the drop and its wake and I_0 a reference pixel intensity correcting the non uniform illumination (obtained from an image with no drop). All image analysis was performed with ImageJ and/or Matlab. The data presented in the main text for both the wake profile (Fig. 4b) and the drop velocity (inset Fig. 6a) were denoised with cubic smoothing splines.

Simulations. Finite element simulations were performed with the commercial software Comsol v5.4. To allow an easier comparison with experiments, the simulations solve the dimensional version of Eq. (1) using the values for our silicone oil, i.e.

$$\frac{\partial h}{\partial t} + \nabla \cdot \left[\frac{h^3}{3\eta} \left(\rho g \cos \alpha \nabla h + \gamma \nabla \kappa + \rho g \sin \alpha \right) \right] = 0,$$

$$\kappa = \nabla \cdot \left[\frac{\nabla h}{\sqrt{1 + \left(\frac{\partial h}{\partial x}\right)^2 + \left(\frac{\partial h}{\partial y}\right)^2}} \right]. \tag{S1}$$

To supply the initial condition $h(x,y,0) = h_0 + h_d(x,y)$ with $h_d(x,y)$ a static pendant drop profile, we solved numerically the Young-Laplace equation with the appropriate boundary
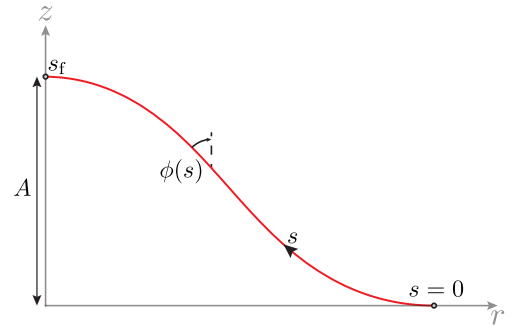

FIG. S1. Schematic of a pendant drop defining the coordinates used for the numerical integration.

conditions [1] using Mathematica (shooting method):

$$\frac{d^2\phi(s)}{ds^2} = \frac{-\cos\phi(s)}{\ell_c^2} + \frac{d}{ds}\left[\frac{\cos\phi(s)}{r(s)}\right]$$

$$\frac{dh_d(s)}{ds} = \cos\phi(s), \quad \frac{dr(s)}{ds} = \sin\phi(s), \quad \text{(S2)}$$

$$h_d(0) = 0, \quad \phi(0) = -\pi/2,$$

$$r(s_f) = 0, \quad \phi(s_f) = -\pi/2, \quad h_d(s_f) = A.$$

Here, $\{r(s), h_d(s)\}$ are the (cylindrical) coordinates of the drop surface, $\phi(s)$ is the local angle that the tangent makes with the vertical and s is the arc-length as defined in Fig. S1. The value of s_f is a priori unknowns and is determined by the additional boundary condition and each profile can be uniquely defined by its amplitude A. The drops shapes are then imported in the FEM solver to be used for the initial condition.

We use rectangular domains with periodic boundary conditions using a square mesh with quadratic Lagrange elements for h and for κ (resolved separately) of size $0.125\ell_c$ or smaller. The simulations shown in Fig. 4-6 have a width $L_y \approx 22.2\ell_c$ and length $L_x \approx 53.3\ell_c$, and were stopped after 10τ or at the onset of dripping ($A > 2.2\ell_c$) or when the drop get too close to the boundary of our simulation domain (distance of the drop maximum to the boundary smaller than $8\ell_c$). The wake profiles $h_w(y)$ were measured between $4.7\ell_c$ and $7\ell_c$ behind the drop center depending on the length of the Landau-Levich region (estimated by looking for $\frac{\partial\kappa}{\partial x}\big|_{y=0} = \text{const}$). As we only focus on quasi-steady moving drop, we discarded the transient initiation of the drop motion (where the drop grows due to the Rayleigh-Taylor instability, see Fig S3) and only present data after the drop has moved by one diameter ($x > 7\ell_c$), when the wake is fully formed. In total 176 simulations are shown in Fig. 4-6 performed with the combination of parameters: $h_0 = \{30, 60, 90, 120\}$ μm, $\alpha = \{0.1, 0.2, 0.3, 0.4, 0.5, 0.6, 0.7, 0.8, 0.9, 1.0, 1.1\}h_0/\ell_c$ with $\ell_c = 1.485$ mm, and four drops profiles $h_d(x,y)$ with initial amplitudes $A_0/\ell_c = \{0.61, 1.0, 1.4, 1.7\}$. The dimensionless values displayed in the main text are therefore relevant to experiments.

II. ADDITIONAL EXPERIMENTAL AND NUMERICAL RESULTS

Experiments at different film thicknesses. The influence of the initial film thickness h_0 is shown in Fig S2(a) where we plot the time evolution of the drop amplitude A for different values of α and h_0. As shown, the quantitative behavior is similar, the timescale on which the growth occurs and the critical angle α_c for the transition are however different. The drop under a quasi-horizontal substrate with $h_0 \approx 55$ μm dripped in 115 min while the one with $h_0 \approx 115$ μm dripped in 45 min, despite being initially 25% smaller. The critical angles vary between $1 \lesssim \alpha_c$ (°) $\lesssim 3$. The same data are plotted in Fig S2(b) but with the time rescaled by $\tau = \eta\gamma/\left(h_0^3\rho^2 g^2 \cos^2\alpha\right)$, the amplitude rescaled by A_0 and the color now coding $\tilde{\alpha}$. As shown this rescaling captures the
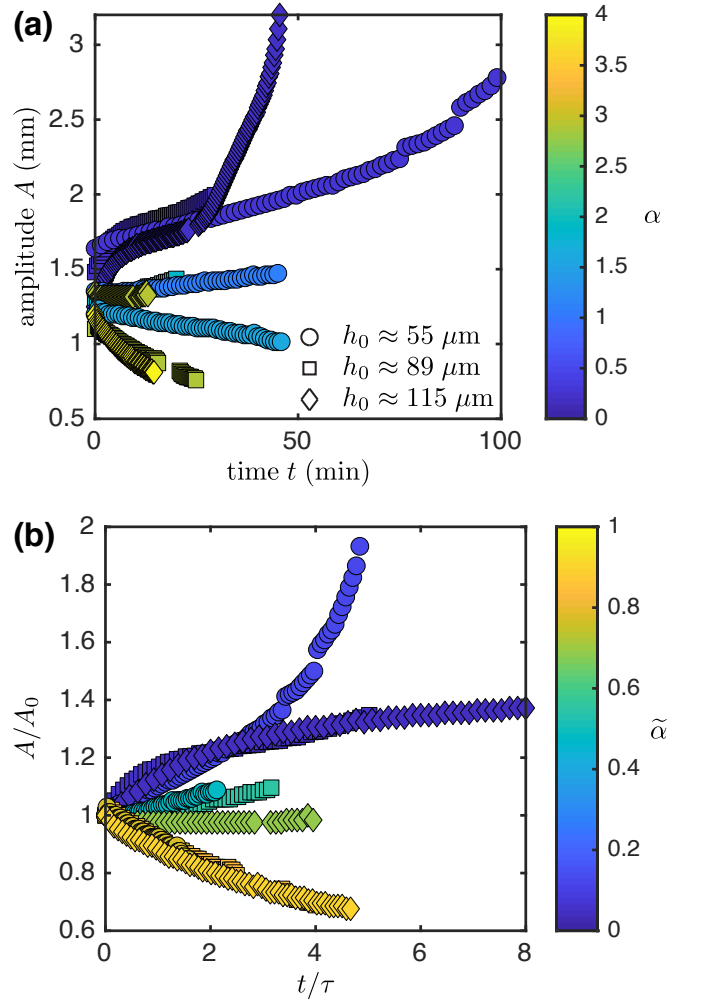

FIG. S2. **(a)** Amplitude A as a function of time t for experimental drops sliding under films of different thicknesses h_0 (see legend) at different inclination angles α (color coded). **(b)** Same data with A rescaled by A_0, time by τ and the color now coding $\tilde{\alpha}$.

change of thickness h_0 for drops of similar initial amplitudes and the critical dimensionless angle is now of the order of $\tilde{\alpha} \approx 0.6$ for all thicknesses. The blue circles, do not collapse probably due to the substantially larger initial drop size in this experiment which accelerate the dynamics.

Influence of the Rayleigh-Taylor instability. For very low inclination angles, we observe in the experiments an initially rapid growth that slows down before increasing again (see Fig 3(a) or Fig. S2). This initial growth and apparent saturation resembles the growth of a motionless drop due to the Rayleigh-Taylor instability [2]. Since drops are always mobile in our experiments, we simulate a motionless one with $\tilde{\alpha} = 0$ and compare it to a drop moving at low inclination angle in Fig. S3. As shown, the initial growth is identical for the two drops until $t \approx 0.5\tau$ the time required for the drop to move by $x \approx \ell_c$. Before, the drop sucks the thin film around it and forms a collar just like an immobile Rayleigh-Taylor
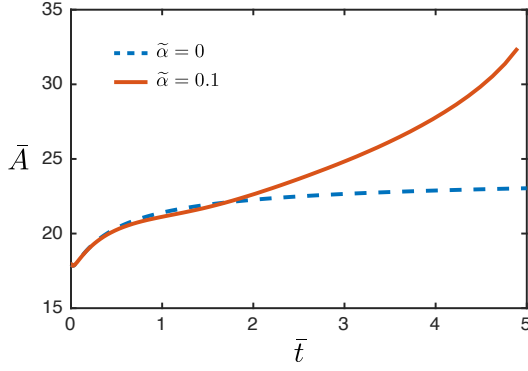
FIG. S3. Dimensionless amplitude $\bar{A}$ as a function of dimensionless time $\bar{t}$ for two simulated drops, one immobile that grows through the Rayleigh-Taylor instability (dashed, $\widetilde{\alpha} = 0$) and the other mobile at very low inclination angle (solid, $\widetilde{\alpha} = 0.1$), film thickness $h_0/\ell_c = 0.06$.
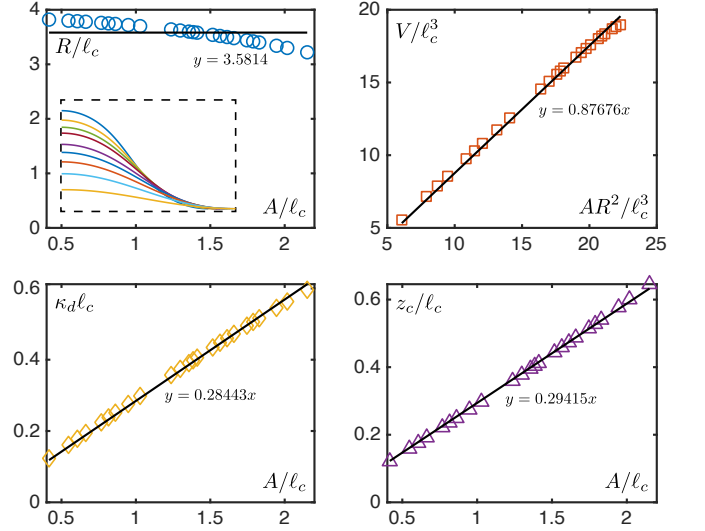

FIG. S4. Properties of pendant drops h_d obtained by numerically solving Eq. (S2) (representative profiles are shown in inset). The black lines are best fits.

drop [3]. The very beginning of the motion is therefore impacted by the non-linear Rayleigh-Taylor dynamics in addition to the dynamic described in this article.

Late time dynamics. Our experiments and simulations only explore the drop dynamics on a domain of roughly $50\ell_c$ (or 15 drop sizes) and we observe growth until dripping below α_c and shrinking above it. At late time, our model suggests this shrinking to go on until complete disappearance of the drop as $A \sim t^{-2}$ [eq. (S11)]. However, the assumption of time scale separation between the Rayleigh-Taylor growth mechanism and the shrinking due to the sliding will eventually break down. Our experimental setup being only 13 cm long, we performed an additional simulation on a much longer domain with a slightly coarser mesh to investigate the long time behavior at high angles ($L_x \approx 220\ell_c$, $A_0/\ell_c = 1.0$, $h_0/\ell_c = 0.06$, mesh size $0.2\ell_c$). The dynamics, shown in Movie S3, turned out to be quite complex. The drop slows down and shrinks as expected, but in the meantime the wake grows due to Rayleigh-Taylor instability and eventually forms small lenses. These lenses then ride the drop wake and eventually catch the drop. However, the volume of these lenses being small and stemming from the drop, the coalescence events barely increase the main drop amplitude. It thus seems unlikely that the drop ends up dripping.

III. THEORY

Justification for the 2D Landau-Levich model. We assume as Lister et al. [3] that the drop moves quasi-steadily at the dimensionless speed $\bar{U}$ and therefore look for traveling wave solutions of eq. (1) of the form $\bar{h}(\bar{x}, \bar{y}, \bar{t}) = \bar{h}(\bar{x} - \bar{U}\bar{t}, \bar{y})$ such that $\frac{\partial \bar{h}}{\partial \bar{t}} = -\bar{U} \frac{\partial \bar{h}}{\partial \bar{x}}$. Equation (1) thus becomes:

$$\bar{\nabla} \cdot \left[\bar{h}^3 \left(\bar{\nabla}\bar{h} + \bar{\nabla}\bar{\kappa}\right)\right] = 3\left(\bar{U} - \widetilde{\alpha}\bar{h}^2\right)\frac{\partial \bar{h}}{\partial \bar{x}}. \qquad \text{(S3)}$$

Now focusing on the annular matching region between the

drop and the thin film [$r \approx R$ in polar coordinates $\{r, \theta\}$, see Fig. 4(c)], we expect small slopes so that we can linearise the curvature $\kappa \approx \nabla^2 h$ which has to vary rapidly to match the drop edge to the thin film. The curvature gradient term dominates the gravitational term (i.e. $\nabla h \ll \nabla^3 h$) and except at the drop side ($\theta = \pm\pi/2$), the azimuthal variations of the curvatures are negligible compared to the radial ones. At leading order, Eq. (S3) therefore becomes [3]:

$$\frac{d}{d\bar{r}}\left[\bar{h}^3 \frac{d^3\bar{h}}{d\bar{r}^3}\right] = 3\left(\bar{U} - \widetilde{\alpha}\bar{h}^2\right)\cos\theta \frac{d\bar{h}}{d\bar{r}}. \qquad \text{(S4)}$$

For small angles, i.e. $\widetilde{\alpha} \ll \bar{U}/\bar{h}^2$, the advection term is negligible and we recover the formulation of Lister et al. [3] that yields the Landau-Levich equation after integrating eq. (S4) once. Since $\bar{h} \sim 1$ in the matching region this condition is equivalent to $\widetilde{\alpha} \ll \bar{U} = \text{Ca}\left(\ell_c/h_0\right)^3 \cos(\alpha)^{-3/2}$ which is of order 10 in our parameter range.

Pendant drop properties. A small slope solution of the Young-Laplace equation which is valid for small static pendant drops writes [3]:

$$\frac{h_d^*(r/\ell_c)}{A} = \frac{J_0(R/\ell_c) - J_0(r/\ell_c)}{J_0(R/\ell_c) - 1}, \qquad \text{(S5)}$$

with A the previously defined drop height, J_0 the Bessel function of the first kind of order 0 and $R \approx 3.8317\ell_c$ the drop radius defined by $J_0'(R/\ell_c) = 0$. Using this approximate solution, we can estimate analytically the numerical prefactors

used in the model:

$$V = 2\pi \int_0^R r h_d^*(r)\,\mathrm{d}r = \frac{\pi J_0(R/\ell_c)}{J_0(R/\ell_c)-1} A R^2 \approx 0.90201 A R^2,$$

$$\kappa_d = \left.\frac{\mathrm{d}^2 h_d^*}{\mathrm{d}r^2}\right|_{r=R} = \frac{J_0(R/\ell_c)}{J_0(R/\ell_c)-1} A \approx 0.28712 A,$$

$$z_c = \frac{1}{2}\frac{\int_0^R r h_d^*(r)^2\,\mathrm{d}r}{\int_0^R r h_d^*(r)\,\mathrm{d}r} = \frac{J_0(R/\ell_c)}{J_0(R/\ell_c)-1} A \approx 0.28712 A.$$

$$\text{(S6)}$$

We further checked these prefactor numerically on the exact pendant drop profiles h_d obtained by solving Eq. (S2). As shown in Fig. S4, except for the drop radius R, these prefactor remain quite accurate even for larger drops. In our model, we use the values fitted on the exact profiles and get the following prefactors c_i:

$$h_w(\theta) = c_h \frac{\ell_c^2}{A}\left(\cos(\theta)\mathrm{Ca}\right)^{2/3}$$

$$c_h = 0.6430 \cdot 3^{2/3}\left(\frac{\kappa_d \ell_c^2}{A}\right)^{-1} \approx 4.7029$$

$$\frac{\partial V}{\partial x} \approx \int_{-R}^{R}(h_0 - h_w(y))\,\mathrm{d}y \approx 2R h_0 - c_v \mathrm{Ca}^{2/3} R\frac{\ell_c^2}{A}$$

$$c_v = c_h \int_{-\pi/2}^{\pi/2} \cos^{5/3}(\theta)\,\mathrm{d}\theta \approx 7.9131$$

$$\mathbf{F_v} = c_F \gamma R \mathrm{Ca}^{2/3}\mathbf{e_x} \qquad \text{(S7)}$$

$$c_F = 4.94 \int_{-\pi/2}^{\pi/2}\cos^{5/3}(\theta)\,\mathrm{d}\theta \approx 8.3121$$

$$\mathrm{Ca}^{2/3} = c_1 \frac{A h_0}{\ell_c^2}\left(1 + c_2\widetilde{\alpha}\right)$$

$$c_1 = \frac{2 z_c/A}{c_F - (z_c/A)c_v} \approx 0.055285$$

$$c_2 = \frac{1}{2}\left(\frac{R}{\ell_c}\right)\left(\frac{V}{A R^2}\right)\left(\frac{z_c}{A}\right)^{-1} \approx 5.3386.$$

We note that we recover the velocity and film thickness prediction of Lister et al. [3] obtained for $\widetilde{\alpha} = 0$ by asymptotically matching the Landau-levitch film to a small slope pendant drop. Our prefactors are however slightly different since they get $c_1' \approx 0.028794$ and $c_v' \approx 7.8350$ after conversion to our notation.

Drop amplitude prediction. By combining Eqs. (3)(4) of the main text we can get a prediction for the drop volume and thus amplitude as a function of time:

$$\frac{\partial V}{\partial t} = U\frac{\partial V}{\partial x} \approx U R h_0\left[2 - c_v c_1\left(1 + c_2\widetilde{\alpha}\right)\right]. \qquad \text{(S8)}$$

From Eq. (S8) we extract the criterion for the growth to decay transition $\widetilde{\alpha}_c = 2/(c_1 c_2 c_v) - 1/c_2 \approx 0.66902$. Then using $U = \gamma \mathrm{Ca}/\eta$ and replacing again Ca with Eq. (4) we get

$$\frac{\partial V}{\partial t} \approx \frac{\gamma}{\eta}c_1^{3/2}\frac{(A h_0)^{3/2}}{\ell_c^3}\left(1 + c_2\widetilde{\alpha}\right)^{3/2}R h_0\left[2 - c_v c_1\left(1 + c_2\widetilde{\alpha}\right)\right],$$
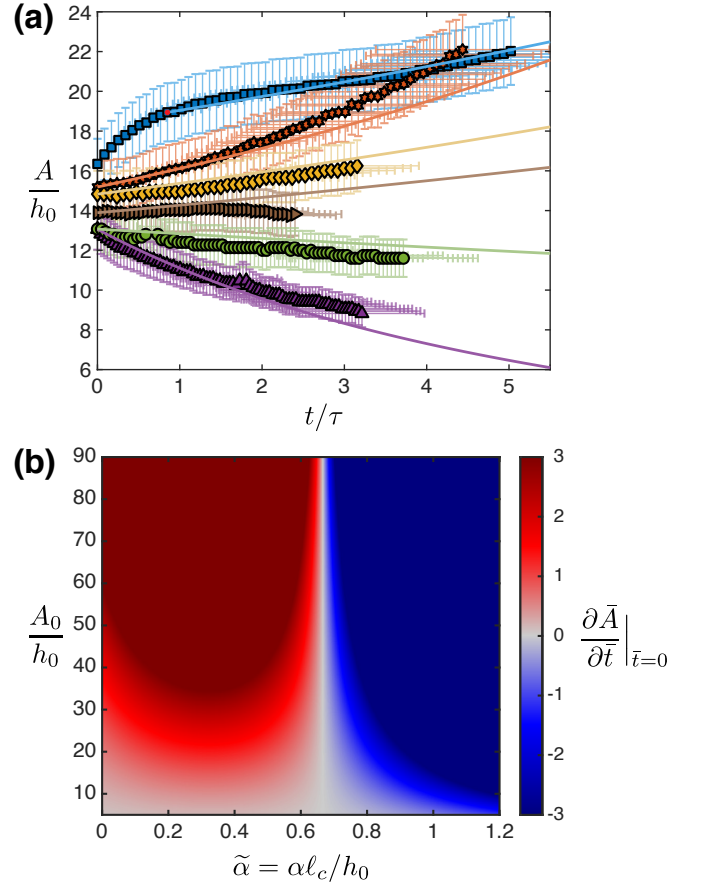
$$\text{(S9)}$$

FIG. S5. **(a)** Dimensionless amplitude as a function of the dimensionless time for the drops of Fig. 3 compared to our theory (solid lines) Eq. (S11). For the lowest inclination angle, the model was compared to experiment after the transient Rayleigh-Taylor growth (see Fig. S3), i.e. using the red circle as initial condition. **(b)** Initial drop dimensionless growth rate map as a function of the dimensionless initial amplitude and $\widetilde{\alpha}$.

which turns into a first order ODE for $A(t)$ after using $V(t) \approx 0.87676 A(t) R^2$ and $R \approx 3.5814\ell_c$. Once made dimensionless by rescaling time with τ and amplitude with h_0 and assuming small slopes such that $\cos\alpha \approx 1$ it reads:

$$\frac{\partial \bar{A}}{\partial \bar{t}} \approx \mathrm{f}(\widetilde{\alpha})\bar{A}^{3/2},$$

$$\mathrm{f}(\widetilde{\alpha}) = \left(\frac{A R^2}{V}\right)\left(\frac{\ell_c}{R}\right)c_1^{3/2}\left(1 + c_2\widetilde{\alpha}\right)^{3/2}\left[2 - c_v c_1\left(1 + c_2\widetilde{\alpha}\right)\right]$$

$$\approx (0.0064682 - 0.0096682\widetilde{\alpha})(1 + 5.3386\widetilde{\alpha})^{3/2}.$$

$$\text{(S10)}$$

Solving Eq. (S10) finally yields the prediction for the amplitude as a function of time

$$\bar{A}(\bar{t}) \approx \frac{\bar{A}_0}{\left(1 - \frac{1}{2}\mathrm{f}(\widetilde{\alpha})\bar{A}_0^{1/2}\bar{t}\right)^2}. \qquad \text{(S11)}$$

We compare Eq. (S11) to the experiment presented in Fig. 3 in Fig. S5(a). Despite all the assumptions of the model,
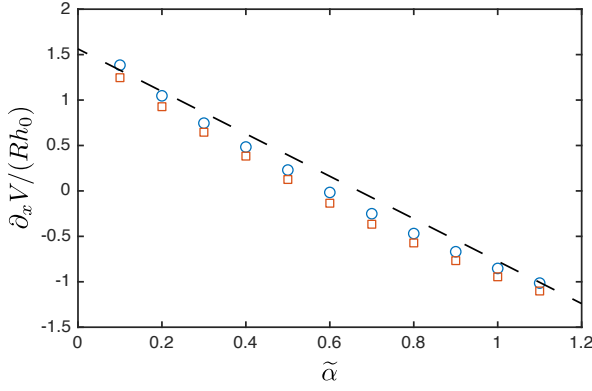
FIG. S6. Change of drop volume $\partial_x V$ normalized by Rh_0 for the simulated wakes of Fig. 5(a). Blue circles include the whole data set including the reconnection to the thin film, i.e. $\int_{-\infty}^{\infty}(h_0 - h_w(y))\,dy$, while orange squares only include the central part of the wake, $\int_{-R}^{R}(h_0 - h_w(y))\,dy$. The dashed line is our model [see eq. (S8)].

FIG. S7. Curvature profiles κ in the flow direction $\bar{x}$ rescaled by the theoretical value in our model $\kappa_d = 0.2844A/\ell_c^2$ for a drop of initial size $A_0/\ell_c = 1.4$ on a film of thickness $h_0/\ell_c = 0.04$ at different inclination angles $\widetilde{\alpha}$ (color coded). All the profiles corresponds to the last time step of each simulation and were shifted horizontally by $\bar{x}_m$, the position of the drop maximum.

the agreement is good except at the beginning of the motion at very low inclination angles due to the Rayleigh-Taylor growth (see Fig. S3). Using Eq. (S10), we construct a theoretical initial growth rate map shown in Fig. S5(b) akin to the phase diagram shown in Fig. 5(b). We recover the independence of the critical angle $\widetilde{\alpha}_c$ with respect to the drop amplitude as well as the steep increase in growth or decay rate as A_0/h_0 increases.

Limitations of the model. In addition to the fact that the advection term stops being negligible in Eq (S4) for larger values of $\widetilde{\alpha}(h_0/\ell_c)^3 Ca^{-1}$, our Landau-Levich analysis has a few other limitations. First as shown in Fig 5(b), our model only predicts the central part of the wake and not the reconnection to the thin film (for $|y| > R$). Using the data of Fig 5(b), we computed the exact volume change $\partial_x V = \int_{-\infty}^{\infty}(h_0 - h_w(y))\,dy$ and the approximate volume change, neglecting the reconnection region $\partial_x V \approx \int_{-R}^{R}(h_0 - h_w(y))\,dy$. As shown in Fig. S6 where both are plotted and compared to our prediction, the
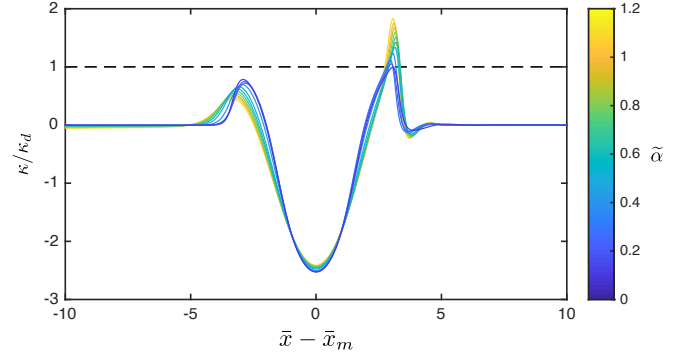
difference is small confirming that the reconnection region is negligible.

Then the pendant drop shapes used for the numerical coefficients (see Fig. S4) are strictly valid for $\alpha = 0$ and $h_0 = 0$. As we increase the angle, we expect the drop shape to vary and even become asymmetric (along x). Fig. S7 shows the horizontal evolution of the curvature $\kappa(x,0)$ as the inclination angle $\widetilde{\alpha}$ increases. At low inclination angles, the drop edge curvature to which the Landau-levich film must connect is close to the one of a static pendant drop κ_d at both the front and the back of the drop. However, as the angle increases the drop shape starts to distort and the edge curvature changes.

Finally, by using the prefactor 4.94 in the friction force $f_v(\theta)$, we implicitly assumed that the drop front and back curvatures were identical [4]. As shown in Fig. S7 the front-back curvature difference also increases with $\widetilde{\alpha}$. This should gradually decrease the value of the prefactor of $f_v(\theta)$ thereby reducing the friction [4], thus possibly explaining why the data is slightly above our prediction at high $\widetilde{\alpha}$.

[1] J. Marthelot, E. F. Strong, P. M. Reis, and P.-T. Brun, Designing soft materials with interfacial instabilities in liquid films, Nature Communications **9**, 4477 (2018).
[2] G. Lerisson, P. G. Ledda, G. Balestra, and F. Gallaire, Instability of a thin viscous film flowing under an inclined substrate: steady patterns, Journal of Fluid Mechanics **898**, A6 (2020).
[3] J. R. Lister, J. M. Rallison, and S. J. Rees, The nonlinear dynamics of pendent drops on a thin film coating the underside of a ceiling, Journal of Fluid Mechanics **647**, 239–264 (2010).
[4] I. Cantat, Liquid meniscus friction on a wet plate: Bubbles, lamellae, and foams, Physics of Fluids **25**, 031303 (2013).